

RESEARCH ARTICLE

10.1002/2015JA021240

Key Points:

- Generation mechanism of substorm-time electric field is investigated
- Differential flux of O^+ ions in the magnetosphere during substorm is simulated
- Nonadiabatic acceleration of O^+ ions results in the rapid energy increase

Correspondence to:

Y. Nakayama,
yohei_nakayama@rish.kyoto-u.ac.jp

Citation:

Nakayama, Y., Y. Ebihara, and T. Tanaka (2015), Generation of large-amplitude electric field and subsequent enhancement of O^+ ion flux in the inner magnetosphere during substorms, *J. Geophys. Res. Space Physics*, 120, 4825–4840, doi:10.1002/2015JA021240.

Received 23 MAR 2015

Accepted 29 MAY 2015

Accepted article online 1 JUN 2015

Published online 25 JUN 2015

Generation of large-amplitude electric field and subsequent enhancement of O^+ ion flux in the inner magnetosphere during substorms

Y. Nakayama¹, Y. Ebihara¹, and T. Tanaka²
¹Research Institute for Sustainable Humanosphere, Kyoto University, Kyoto, Japan, ²International Center for Space Weather Science and Education, Kyushu University, Fukuoka, Japan

Abstract Energetic O^+ ions are rapidly enhanced in the inner magnetosphere because of abrupt intensification of the dawn-to-dusk electric field and significantly contribute to the ring current during substorms. Here we examine the generation mechanism of the dawn-to-dusk electric field that accelerates the O^+ ions and the spatial and temporal evolution of the differential flux of the O^+ ions by using a test particle simulation in the electric and magnetic fields that are provided by a global magnetohydrodynamics (MHD) simulation. In the MHD simulation, strong dawn-to-dusk electric field appears in the near-Earth tail region by a joint action of the earthward tension force and pileup of magnetic flux near an onset of substorm expansion. The peak of the electric field is ~ 9 – 13 mV/m and is located ~ 1 – $2 R_E$ earthward of the peak of the plasma bulk speed because of the pileup. O^+ ions coming from the lobe are accelerated from \sim eV to >100 keV in ~ 10 min. The reconstructed flux of the O^+ ions shows that at $\sim 7 R_E$ near midnight, the flux has a peak near a few tens of keV and the flux below ~ 10 keV is small. This structure, called a “void” structure, is consistent with the Polar observation and can be regarded as a manifestation of the acceleration of unmagnetized ions perpendicular to the magnetic field. In the inner magnetosphere (at $6.0 R_E$), reconstructed energy-time spectrograms show the nose dispersion structure that is also consistent with satellite observations.

1. Introduction

O^+ ion is one of the major ion species in the magnetosphere [e.g., Shelley *et al.*, 1972; Lennartsson *et al.*, 1979; Kistler *et al.*, 1989; Daglis and Axford, 1996; Moore *et al.*, 1997; Elliott *et al.*, 2007; Kistler *et al.*, 2010; Liao *et al.*, 2010]. Observations have shown that the O^+ ions are widely distributed in the magnetosphere, such as the plasma sheet, the lobe, the mantle, and the inner magnetosphere [e.g., Young *et al.*, 1982; Lundin *et al.*, 1982; Krimigis *et al.*, 1985; Hamilton *et al.*, 1988; Moore *et al.*, 1997; Nose *et al.*, 2001; Nilsson *et al.*, 2004]. The exclusive source of the O^+ ions is thought to be the Earth’s ionosphere [Moore and Delcourt, 1995; Moore *et al.*, 2001] because the O^+ ions are not observed in the solar wind. The O^+ ions outflowing from the ionosphere are grouped into four categories: polar wind, auroral bulk O^+ upflow, ion beams, and ion conics, according to energy and pitch angle distributions, as summarized in Moore *et al.* [1999]. The polar wind flows from the polar cap region and is characterized by O^+ ions with thermal energy on the order of eV. Auroral bulk O^+ upflow frequently occurs in the topside auroral ionosphere (~ 500 km) at velocities of 100–1000 m/s or greater. Ion beams and ion conics are manifestations of acceleration processes where all or only a fraction of the ions are energized. Both ion beams and ion conics have energy in the 10 eV to few keV range.

A notable feature of the O^+ ions in the inner magnetosphere is their drastic enhancement in accordance with geomagnetic activities [e.g., Young *et al.*, 1982; Hamilton *et al.*, 1988; Roeder *et al.*, 1996; Daglis and Axford, 1996; Daglis, 1997] and fast plasma flows in the near-Earth tail [Zong *et al.*, 1997; Ohtani *et al.*, 2015]. Data from the Active Magnetospheric Particle Tracer Explorers/Charge Composition Explorer show that the contribution from the O^+ ion to the total ion energy density increases at geosynchronous altitude when the AE index is high [Daglis *et al.*, 1993] and that the bulk of the ion energy density comes from the high-energy component of O^+ (17–300 keV) in comparison with the low-energy one (1–17 keV) after the substorm onset [Daglis and Axford, 1996]. Fu *et al.* [2002] identified rapid flux intensifications of the O^+ ions in the inner magnetosphere during substorm-associated injection events based on the data from the Combined Release and Radiation Effects Satellite (CRRES). One typical observation result showed that in

the premidnight sector, the O^+ ion flux in the energy range of >50 keV increases within 5 min after a substorm expansion onset and the increase in the flux lasted about 30 min. Snapshots of energetic neutral oxygen emitted from the energetic O^+ ions had been observed by Imager for Magnetopause-to-Aurora Global Exploration/High Energy Neutral Atom (IMAGE/HENA). Energetic neutral oxygen with energy between ~ 50 and ~ 200 keV was observed to be rapidly enhanced in the inner magnetosphere at almost the same time as auroral substorms [Mitchell *et al.*, 2003; Ohtani *et al.*, 2007; Keika *et al.*, 2010]. Mitchell *et al.* [2003] analyzed bursts of energetic neutral oxygen observed by IMAGE/HENA. They suggested that local acceleration of preexisting O^+ ions in the near-Earth plasma sheet is responsible for the observed O bursts because the time delay between substorm expansion onset and the O burst in the inner magnetosphere ($3\text{--}5 R_E$) is short (~ 20 min).

The rapid appearance of the O^+ ion with energy on the order of 100 keV in the inner magnetosphere can be explained by the acceleration and transport of the O^+ ions in the near-Earth plasma sheet during a dipolarization [e.g., Delcourt, 2002; Fok *et al.*, 2006; Ashour-Abdalla *et al.*, 2009; Peromian *et al.*, 2011; Birn *et al.*, 2013]. Delcourt [2002] investigated the processes by using a test particle simulation. To model electric and magnetic fields associated with a dipolarization, he introduced the magnetic field given by interpolating two states of the empirically obtained magnetic field and the electric field obtained by the time derivative of the vector potential. The result shows that an O^+ ion with initial energy of ~ 10 eV in the equatorial plane is accelerated to ~ 100 keV as it encounters the dipolarization when it moves from $L=9.0$ to $L=6.8$. An O^+ ion with an initial energy of 100 eV was also launched from the auroral zone on the nightside. The kinetic energy is increased to ~ 100 keV when dipolarization is introduced, whereas the energy is increased only to ~ 10 keV for the absence of the dipolarization. Fok *et al.* [2006] performed a test particle simulation under the electric and magnetic fields obtained by a global magnetohydrodynamics (MHD) simulation and concluded that direct injection of cold O^+ ions from the ionosphere will result in a significant time lag between the onset of the O^+ outflow and the enhancement in the inner magnetosphere. This means that direct injection of cold O^+ from the ionosphere is unlikely to explain the burst of the energetic neutral oxygen measured by IMAGE/HENA. Fok *et al.* [2006] pointed out that nonadiabatic acceleration of preexisting O^+ ions can account for the O^+ burst without introducing direct injection of O^+ ions from the ionosphere. Nakayama *et al.* [2014] investigated the acceleration of the O^+ ions in the azimuthally directed magnetic field line that is formed in the near-Earth plasma sheet just before the substorm onset. Their result showed that the azimuthally directed magnetic field line is easily formed during substorm under the presence of the Y component of interplanetary magnetic field (IMF) and that O^+ ions are effectively accelerated from ~ 1 keV to ~ 100 keV when passing through that region.

It is also accepted that a nonadiabatic acceleration triggered by dipolarization contributes the rapid energization of O^+ ions [Delcourt *et al.*, 1990, 1991; Delcourt and Moore, 1992; Delcourt, 2002]. The nonadiabatic acceleration occurs when a Larmor radius of charged particle is comparable to the curvature radius of the magnetic field line. This process easily happened for O^+ ions because heavy O^+ ions have a large Larmor radius as compared with light ion in the magnetosphere like H^+ and He^+ . This can explain the observations that O^+ ions are more effectively accelerated than H^+ and He^+ ions during the substorms [Fu *et al.*, 2002; Mitchell *et al.*, 2003; Ohtani *et al.*, 2005].

Many studies have pointed out the importance of the dawn-to-dusk electric field in the near-Earth plasma sheet and nonadiabatic acceleration during the depolarization for the rapid generation of energetic O^+ ions associated with a substorm. However, at least two questions remain unanswered. The first question is the generation mechanism of the dawn-to-dusk electric field that rapidly accelerates the O^+ ions to the energy on the order of 100 keV. The second question is the evolution of the distribution function (or the differential flux) of the O^+ ions as a function of position, energy, and time. To answer these questions, we performed a test particle simulation in the electric and magnetic fields obtained by a global MHD simulation and reconstructed the distribution function of the O^+ ions.

2. Observation of Energy Spectrum of O^+

Fu *et al.* [2002] showed three examples of counting rates of O^+ ions observed by CRRES during substorms as a function of energy and time. At $L < 6.6$ near the equatorial plane, the counting rates of the O^+ ions increase at

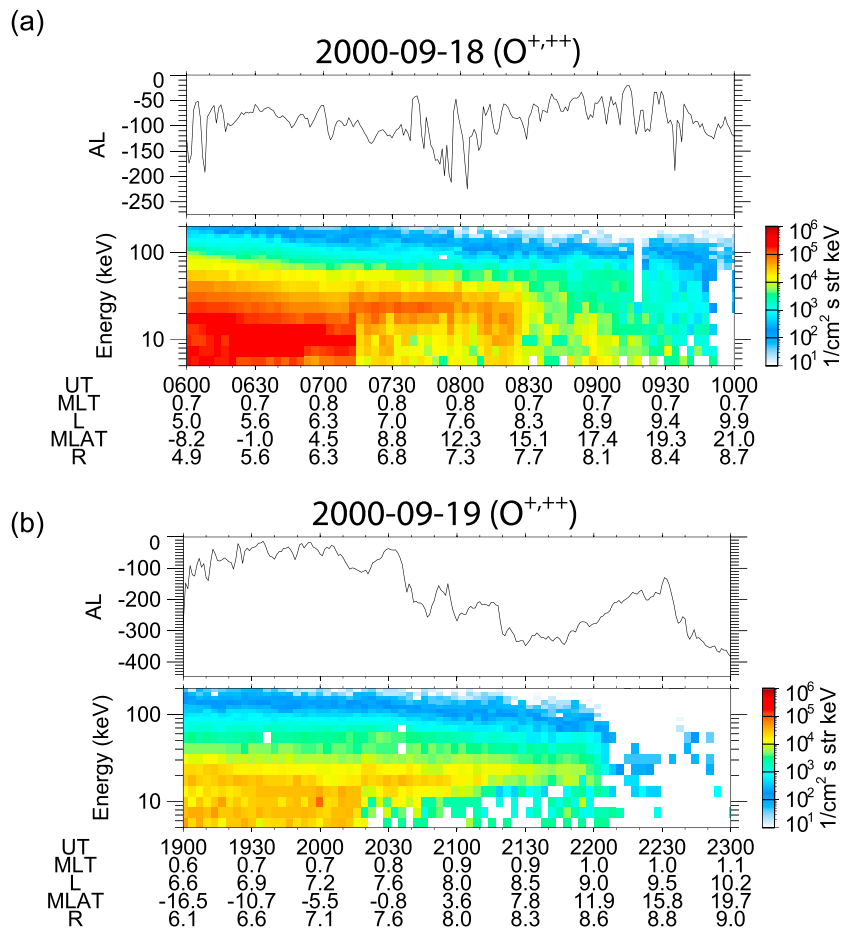


Figure 1. Differential flux of the O^{+} ions taken by the Polar satellite at $L \sim 6.6$ – 9.0 near midnight near the equatorial plane. Ephemeris information is included at the bottom of the figure. MLT represents the magnetic local time in hours, magnetic latitude represents the magnetic latitude in degrees, and R represents the geocentric distance in R_E .

all energy. The increase of the counting rates has a delay depending on energy. That is, an energy-time dispersion appears. Sometimes drift echo appears in accordance with the drift period of the O^{+} ions. In the near-Earth plasma sheet, the response of the O^{+} ions is different from that in the inner magnetosphere. Figure 1 shows two examples of the differential flux of the O^{+} ions taken by magnetospheric ion composition spectrometer (MICS) onboard the Polar satellite [Wilken *et al.*, 1992]. The Polar satellite was launched into an elliptical orbit with an apogee of $9 R_E$, a perigee of $2 R_E$, and inclination of 86° . Two examples were obtained at $L \sim 6.6$ – 9.0 near midnight near the equatorial plane. In both cases, the Polar satellite moved outward from the Southern Hemisphere to the Northern Hemisphere. The differential flux of the O^{+} ions is kept relatively high in the entire energy range between 5 keV and 200 keV for the first one-third period. During this period, the flux sharply decreases with energy. During the second one-third period (between 07:15 UT and 08:10 UT in Figure 1a; between 20:13 UT and 22:00 UT in Figure 1b), the flux below 10 keV significantly decreases. The flux has a peak at 15–30 keV. We discuss the feature of flux decrease at low energies and its generation mechanism later.

3. Simulation

3.1. Global MHD Simulation

We used a global MHD simulation developed by Tanaka *et al.* [2010] to derive the electric and magnetic fields associated with a substorm self-consistently. Two different boundary conditions in the solar wind were used, which are summarized in Table 1. In Case I, the solar wind speed was held constant to be 372 km/s

Table 1. Solar Wind Parameters That Are Used as Boundary Conditions in the MHD Simulation

	Solar Wind Speed (km/s)	IMF (nT)
Case I	372	(0, 2.5, 4.33) → (0, 4.33, −4.33)
Case II	500	(0, 2.5, 5.0) → (0, 2.5, −5.0)

and IMF turned from (0, 2.5, 4.33) to (0, 4.33, −4.33) nT. In Case II, the solar wind speed was held constant to be 500 km/s and IMF turned from (0, 2.5, 5.0) to (0, 2.5, −5.0) nT. The simulation settings for Case I are the same as those used by *Ebihara and Tanaka*

[2013]. The onset of substorm expansion phase is defined as the moment at which the calculated AL index suddenly decreases and hereinafter referred to as $t=0$.

3.2. Test Particle Simulation

Since our primary focus is on the acceleration and transport processes of the O^+ ions in near-Earth tail region, we started tracing the ions at off-equator where cold O^+ stream outflowing from the ionosphere is dominant. We introduced two planes parallel to the equatorial plane $Z = \pm 2 R_E$, ranging from $X = -7$ to $-17 R_E$ and from $Y = -10$ to $10 R_E$. We divided the plane into 10×20 Cartesian grid cells, and each grid cell has $1 R_E$ width (ΔX_i) and $1 R_E$ length (ΔY_i). The geometry of the grid cells is shown in Figure 2. O^+ ions were placed at the grid points ($11 \times 21 \times 2$ in total) with an interval time Δt of 1 min. In velocity space, we introduced spherical coordinates: kinetic energy, polar angle θ (the angle between the velocity vector and the Z axis), and azimuthal angle ϕ (the angle between the velocity vector and the Sun projected on the X - Y plane). Initial kinetic energy K_i is defined in the frame of the bulk velocity simulated by global MHD simulation, and it is logarithmically divided as

$$K_i = 10^{0.3h} \text{ eV}, \quad h = 0 \text{ to } 10.$$

Thus, K_i ranges from 1 eV to 1 keV with a constant interval in logarithmic scale. We added the ions with $K_i = 0$ eV because these ions have the bulk velocity in the inertial frame of reference. Initial polar angle θ_i is divided linearly from 90° to 180° in the Northern Hemisphere and 0° to 90° in the Southern Hemisphere with an interval of 1° . Initial azimuth angle ϕ_i is also divided linearly from 0° to 360° with an interval of 10° . In total, a few billion test particles were traced from the planes for each case. The scheme for test particle tracing is the same as that described by *Nakayama et al.* [2014].

We calculated the distribution function f in accordance with Liouville's theorem. Each test particle carries the real number of particles ΔN in the small bin in the six-dimensional space (three dimensions in the configuration space and three dimensions in the velocity space) as

$$\Delta N = f_i \Delta^3 r_i \Delta^3 v_i, \quad (1)$$

where $\Delta^3 r_i$ and $\Delta^3 v_i$ are the volumes in configuration space and velocity space, respectively, which are represented by

$$\Delta^3 r_i = v_i \cos \theta_i \Delta X_i \Delta Y_i \Delta t, \quad (2)$$

$$\Delta^3 v_i = v_i^2 \sin \theta_i \Delta v_i \Delta \theta_i \Delta \phi_i, \quad (3)$$

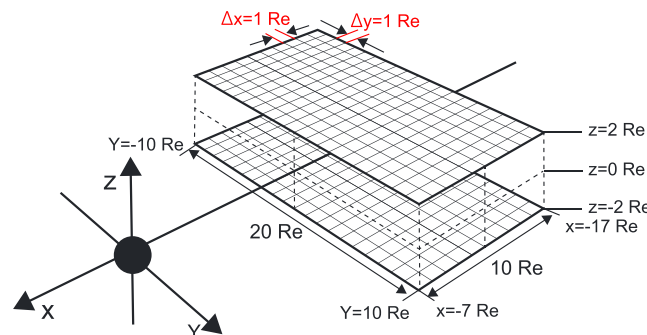


Figure 2. The geometry of the grid cells that are used to place test particles.

where v_i is the corresponding velocity of particle to K_i , that is $\sqrt{2K_i/m}$. After tracing particles, we reconstructed f by accumulating the real number of the particles falling into a small bin in configuration space and velocity space,

$$f = \frac{\sum \Delta N}{\Delta^3 r \Delta^3 v}. \quad (4)$$

Reader may refer *Ebihara et al.* [2006] for more detailed information about the methodology. In this particular study,

we assumed a drifting Kappa distribution in the source region. The drifting Kappa distribution is modified from the original Kappa distribution [Vasyliunas, 1968; Summers and Thorne, 1991] as

$$f_i = \frac{n}{\pi^{3/2} \theta^3} \frac{\Gamma(\kappa + 1)}{\Gamma(\kappa - 1/2)} \left(1 + \frac{(\mathbf{v} - \mathbf{V}_{\text{MHD}})^2}{\kappa \theta^2} \right)^{-(\kappa + 1)} \quad (5)$$

and

$$\theta = \frac{2\kappa - 3}{\kappa} \frac{kT}{m}, \quad (6)$$

where n , κ , k , m , \mathbf{v} , T , and \mathbf{V}_{MHD} are the density, the spectral index, the Boltzmann constant, the mass of particle, the velocity of particle, the temperature, and the bulk velocity of plasma given by the MHD simulation. We assumed that $n = 0.1 \text{ cm}^{-3}$, $\kappa = 4.5$, and $kT = 10 \text{ eV}$ unless otherwise mentioned. In order to compare with satellite observations, we calculated the directional differential flux j as

$$j = \frac{v^2}{m} f. \quad (7)$$

4. Result

4.1. Global MHD Simulation

4.1.1. Case I

Figure 3 summarizes the key quantities obtained by the MHD simulation in the equatorial plane at the onset of the substorm expansion. Our MHD simulation result showed that the formation of the near-Earth neutral line (NENL) in the midtail region causes the earthward fast flow. The earthward flow corresponds to the transient electric field. The earthward flow results in the plasma squeezing and the formation of high-pressure region in the inner magnetosphere. Then the AL starts to decrease [Tanaka et al., 2010]. Figure 3a shows the plasma pressure. The plasma pressure has a peak around 7–9 R_E near midnight. There is a subpeak in the pressure around 10 R_E near midnight. Figure 3b shows the Y component of the electric field E_y . The dawn-to-dusk electric field is significantly enhanced at $>8 R_E$ in longitudinally narrow regions in the premidnight and postmidnight. The regions where the strong E_y occurs are determined by the NENL; however, we do not have the answer to the question why the NENL formed in longitudinally narrow regions. The strongest E_y occurs between 8 and 9 R_E . Figure 3c shows the X component of the plasma bulk flow (V_x), indicating that fast earthward flow (positive V_x) is established between 11 and 15 R_E . The region where V_x is largest is located farther away from the Earth than where E_y is the largest. Figure 3d shows the magnetic field strength. There is a subpeak in the magnetic field strength between 9 and 10 R_E near midnight. The subpeak can be explained in terms of pileup of the magnetic flux associated with dipolarization. Figure 3e shows the curvature radius of a magnetic field line. Near midnight, the curvature radius is, in general, small ($<1 R_E$) except around 10 R_E . The right-hand side of Figure 3 summarizes the force density in the X component. In the ideal MHD, the balance of the force density is given by

$$\rho \frac{d\mathbf{v}}{dt} = -\nabla P + \mathbf{J} \times \mathbf{B} \quad (8)$$

$$\mathbf{J} \times \mathbf{B} = \frac{(\mathbf{B} \cdot \nabla) \mathbf{B}}{\mu_0} - \nabla \left(\frac{B^2}{2\mu_0} \right), \quad (9)$$

where ρ is the mass density, μ_0 is the magnetic constant, \mathbf{J} is the current density, P is the plasma pressure, and \mathbf{B} is the magnetic field. The left-hand side of equation (8) is called inertial force, which is shown in Figure 3f. Two terms on the right-hand side (RHS) of equation (8) are called plasma pressure force (Figure 3g) and Lorentz force (Figure 3h), respectively. The Lorentz force can be divided into two as equation (9). Two terms on the RHS of equation (9) are called tension force (Figure 3i) and magnetic pressure force (Figure 3j), respectively. The X component of tension force and magnetic pressure force is written as $\frac{(\frac{\partial B_x}{\partial x} + \frac{\partial B_y}{\partial y} + \frac{\partial B_z}{\partial z}) B_x}{\mu_0}$ and $-\frac{\partial}{\partial x} \left(\frac{B^2}{\mu_0} \right)$, respectively. In Figure 3i and 3j, the sign is different between nightside and dayside because the sign of B_x and $-\frac{\partial}{\partial x} \left(\frac{B^2}{\mu_0} \right)$ is opposite. There are three characteristics to be noted regarding the force density. First, earthward (tailward) inertial force is established earthward (tailward) of the NENL that is located at $\sim 14 R_E$ near midnight (Figure 3f). The earthward inertial force is

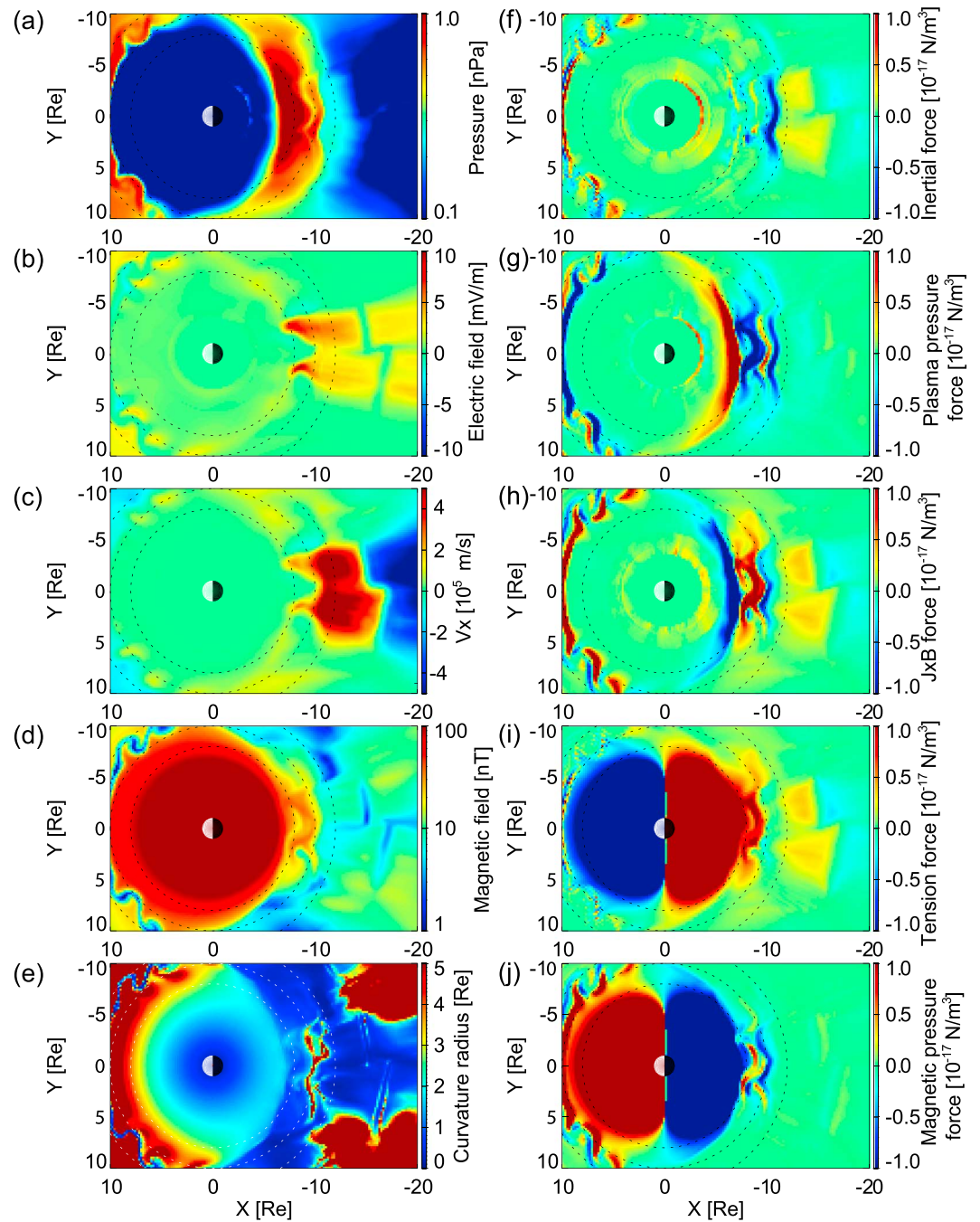


Figure 3. (a) The plasma pressure, (b) the Y component of the electric field E_y , (c) X component of the plasma bulk flow V_x , (d) the magnetic field strength, (e) the curvature radius of a magnetic field line, (f) the inertial force, (g) the plasma pressure force, (h) the Lorentz force, (i) the tension force, and (j) the magnetic pressure force in the X component in the equatorial plane at $t = 0$ min for Case I. The sum of the Lorentz force and the plasma pressure force is equal to the inertial force.

due to the dominance of the tension force that is shown in Figure 3i. The earthward inertial force results in the increase in V_x (Figure 3c) and hence the increase in E_y (Figure 3b). Second, at $\sim 10 R_E$ near midnight, tailward inertial force becomes dominant as shown by bluish color in Figure 3f. The tailward inertial force is caused by the plasma pressure force (Figure 3g) and the magnetic pressure force (Figure 3j). Third, in a narrow region at $\sim 9 R_E$ in the midnight, the earthward inertial force becomes dominant again, which results from the earthward tension force (Figure 3i).

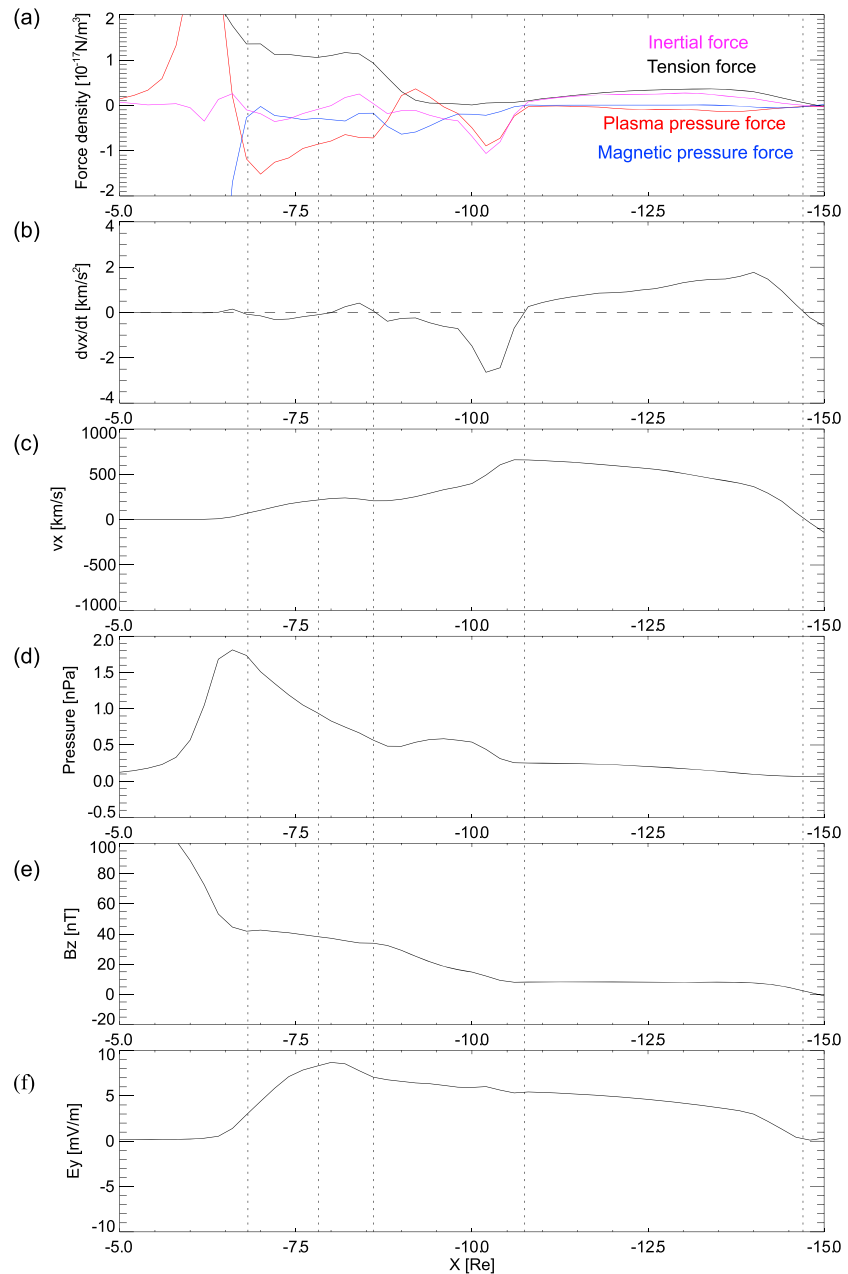


Figure 4. (a) The X component of the force densities. Summation of the plasma pressure force, the tension force and the magnetic pressure force is equal to the inertial force. (b) The acceleration of the plasma bulk flow, (c) V_x , (d) the plasma pressure, (e) the Z component of the magnetic field B_z , and (f) E_y , at $Y = -2.5 R_E$ in the equatorial plane as a function of X for Case I.

Figure 4 summarizes the selected quantities at $Y = -2.5 R_E$ in the equatorial plane as a function of X . The vertical black dotted lines indicate the position where the inertial force density is zero. In the region between $X = -10.8$ and $-14.5 R_E$, the inertial force density is earthward because of the dominance of the earthward tension force (Figure 4a) and the plasma is accelerated earthward (Figure 4b). In the region between $X = -8.6$ and $-10.8 R_E$, the inertial force density is tailward (Figure 4a) and the plasma is decelerated (Figure 4b). The deceleration of the plasma flow comes from the tailward plasma pressure force and the magnetic pressure force (Figure 4a). Thus, the earthward flow velocity has a peak at $X = -10.5 R_E$ (Figure 4c). The Z component of the magnetic field (B_z) increases with X , which can be regarded as the pile up of the magnetic flux in association with the flow braking (Figure 4e). In the region

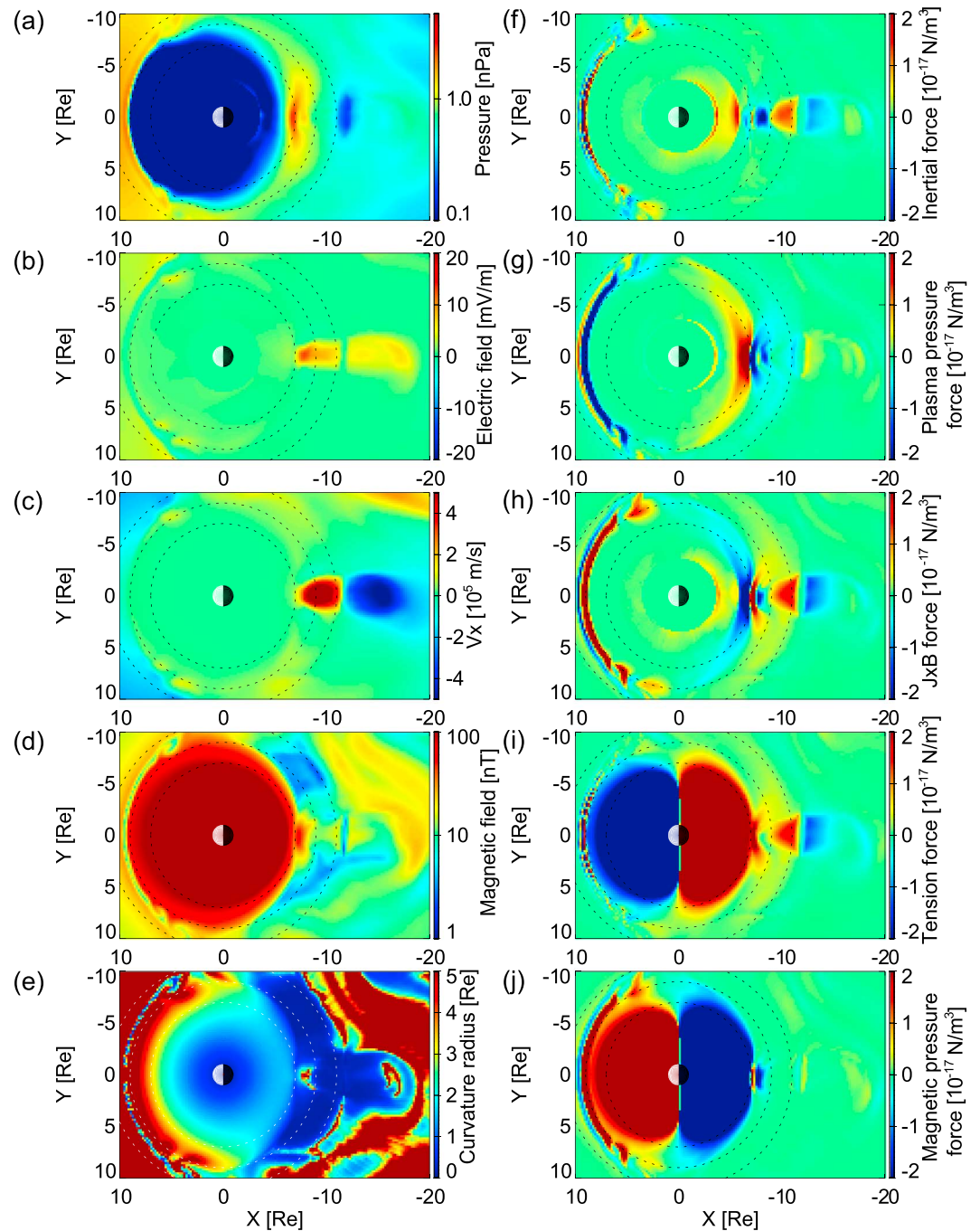


Figure 5. Same as Figure 3 except for Case II.

between $X = -8.0$ and $-8.6 R_E$, the inertial force density is slightly positive (Figure 4a) and the earthward flow velocity is almost constant (Figure 4c). However, E_y increases with X and has a peak at $X = -8.0 R_E$. This is simply understood to the fact that in the ideal MHD, the electric field is given by the following equation,

$$\mathbf{E} = -\mathbf{V} \times \mathbf{B}. \quad (10)$$

Thus, the peak of E_y takes place $2.5 R_E$ earthward of the peak of V_x .

4.1.2. Case II

Key quantities for Case II are summarized in Figure 5. The overall distributions of the quantities are essentially same as that for Case I. Noticeable differences between Case I and Case II are the location of the NENL and the

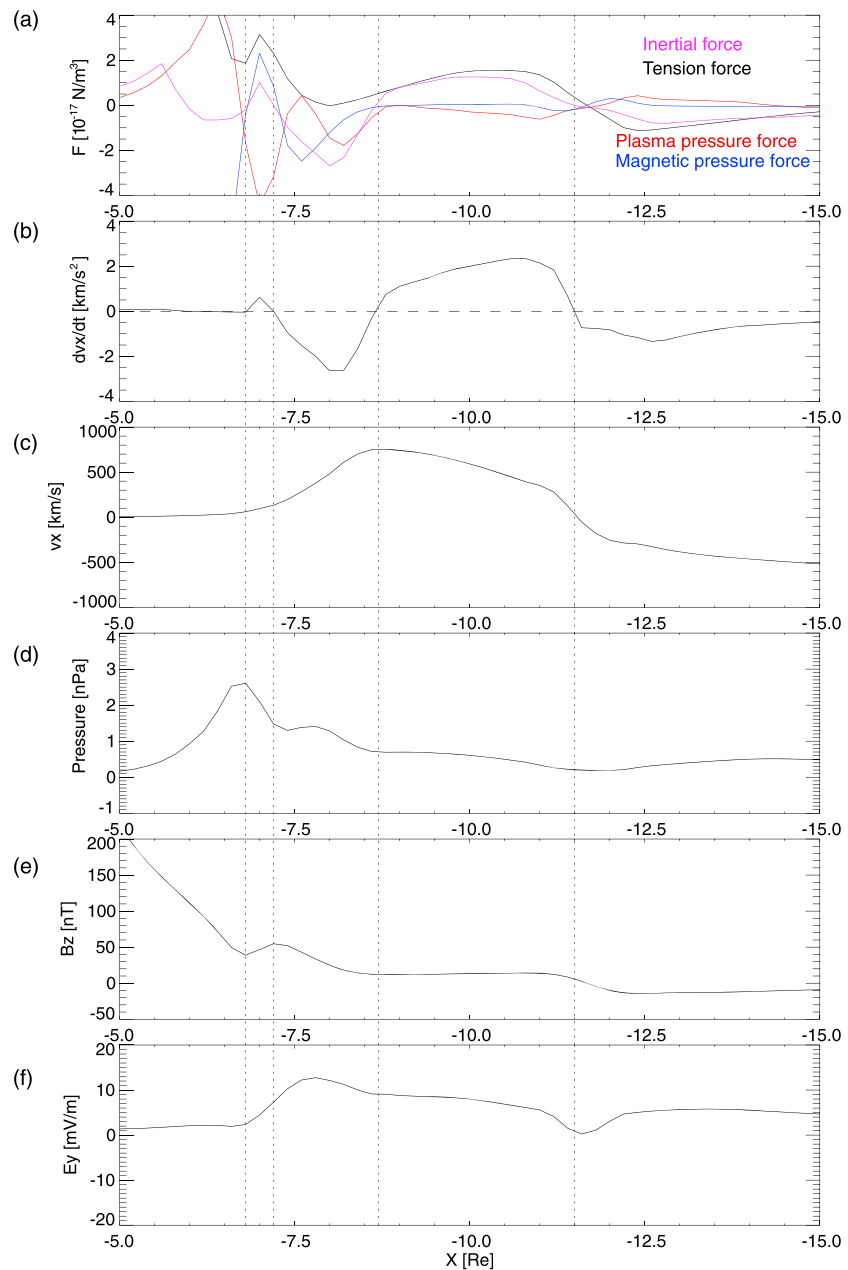


Figure 6. Same as Figure 4 except at $Y = 0 R_E$ in the equatorial plane as a function of X except for Case II.

intensity of E_y . The NENL is formed at $\sim 11.5 R_E$ near midnight, which is $2.5 R_E$ earthward of the NENL for Case I. The peak of E_y is ~ 13 mV/m for Case II (Figure 5b), whereas that is ~ 9 mV/m (Figure 3b).

Figure 6 is the same as Figure 4 except for Case II at $Y = 0 R_E$. The mechanism of the enhancement of E_y is essentially the same as that of Case I. The peak of E_y occurs $1 R_E$ earthward of the peak of V_x because of pileup of the magnetic flux.

4.2. Test Particle Simulation

4.2.1. Case I

Figure 7 summarizes snapshots of the differential flux j of the O^+ ions at three energy intervals from 10 to 50 keV (top row), 50 to 100 keV (middle row), 100 to 200 keV (bottom row) at $t = -5$ (first column), 0 (second column), and 5 (third column) min. A white contour line indicates the region where $|E_y|$ is 5 mV/m. At the onset and onward, there are, at least, two distinct areas where $|E_y|$ is greater than 5 mV/m

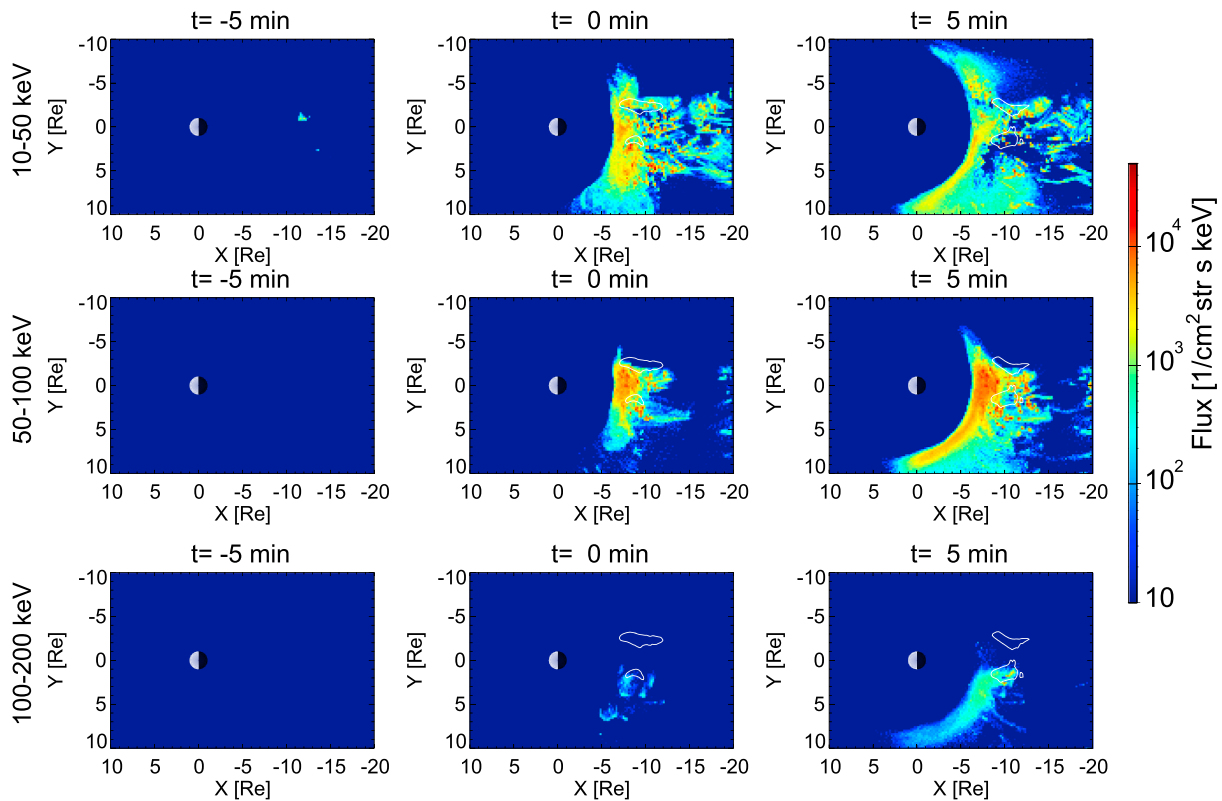


Figure 7. Snapshots of the differential flux j of the O^+ ions at three energy intervals from (top row) 10 to 50 keV, (middle row) 50 to 100 keV, and (bottom) 100 to 200 keV at (first column) $t = -5$, (second column) 0, and (third column) 5 min. The white contour line indicates the region where $|E_y|$ is 5 mV/m.

in the premidnight and postmidnight regions. At $t = -5$ min (first column), the flux remains low at all energy intervals. At the substorm onset ($t = 0$; second column), the flux at all the energy intervals is suddenly enhanced on the nightside. The region where the flux is high occupies from 7 to, at least, $20 R_E$ in azimuthally wide area on the nightside. The significant enhancement of the flux takes place at $Y \geq -3 R_E$. This implies that significant acceleration of the O^+ ions takes place the region where $|E_y|$ is large and that the flux at high energy increases just westward of the high E_y region. At $t = 5$ min (third column), the region where the flux is high propagates duskward because the ions drift westward due to the grad-B and curvature drift. After encircling the Earth, the ions came back to midnight (not shown) and contribute to the drift echo structure as mentioned later.

To understand the acceleration and transport process of the O^+ ions with energy greater than 100 keV, we focused on the 42 most significant test particles that contribute to the flux j at the energy interval from 100 to 200 keV at $X = -7.5 R_E$ and $Y = -2.0 R_E$. In total, they contribute to 5% of the flux j at that point. Figure 8 shows the trajectories of the 42 test particles in the X - Y and X - Z planes. The kinetic energy of the ion is indicated by color. The contour lines in Figure 8a indicate $|E_y|$ at $t = 0$. The black lines in Figure 8b indicate the magnetic field lines extending from $X = -4$ to $-16 R_E$ at $Y = -2.5 R_E$ at $Z = 0 R_E$ at $t = 0$. All the ions are found to depart at $(-13, -4, 2) R_E$ at $t = -4$ min with initial energy of around 5 eV. Because initial time, position, and energy of the O^+ ions are same and initial polar and azimuth angle are similar, they show similar trajectories and energy increases. After the departure, the O^+ ions move tailward and toward the equatorial plane. The kinetic energy is not significantly increased. When these ions reach the earthward vicinity of the NENL ($X \sim -14.5 R_E$) near the equatorial plane, and the direction of the ion velocity turns from tailward to earthward (Figure 8b), immediately after the changing of the direction, they proceed earthward and the kinetic energy increases. Finally, the energy reaches 120 keV. The bottom plot of Figure 8 shows kinetic energy as a function of time, which shows a two-step increase. The increases in energy occurs when the ions traverse the region where $|E_y|$ is large. During the first increase, the energy increases to 65 keV, and during the second increase, it increases to 120 keV.

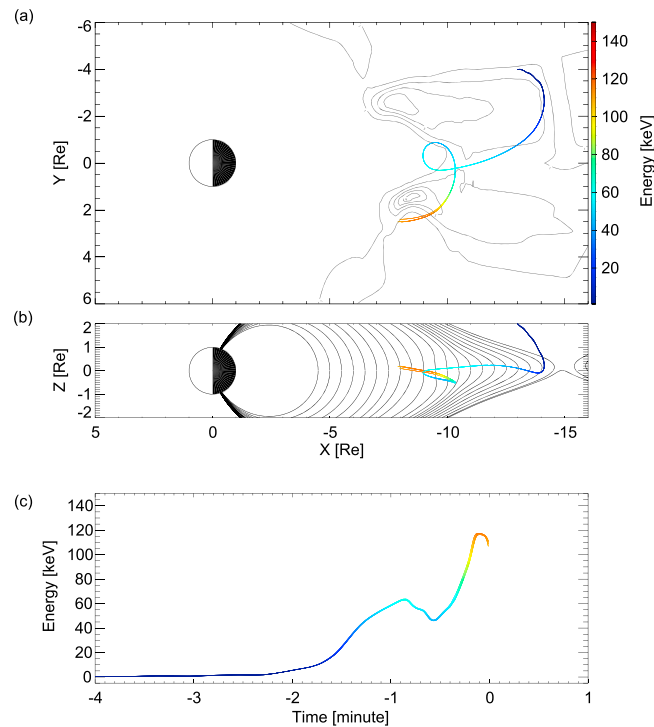


Figure 8. The trajectories of the 42 test particles in the (a) X-Y and (b) X-Z planes with energy color coded. The black lines in Figures 8a and 8b represent $|E_y|$ contours and magnetic field lines, respectively. (c) The kinetic energy as a function of t .

We calculated the ratio $K = R_{\text{cmin}}/\rho_{\text{Lmax}}$ where R_{cmin} is the minimum curvature radius of a magnetic field and ρ_{Lmax} is the maximum Larmor radius of a particle [Sergeev *et al.*, 1983]. Sergeev *et al.* [1983] have pointed out that a charged particle undergoes non-adiabatic motion when $K < 8$. At $X = -13 R_E$ and $Y = 0 R_E$ (in which the first increase in energy takes place), the curvature radius of the magnetic field line is $0.2 R_E$, and the magnetic field strength is 8.1 nT. The Larmor radius of the O^+ ion with energy of 40 keV is $2.2 R_E$, so that $K = 0.09$. At $X = -10 R_E$ and $Y = 1.5 R_E$ (in which the second increase in energy takes place), K is calculated to be 0.7 for the O^+ ion with energy of 226 keV. Thus, it is obvious that the O^+ ions undergo nonadiabatic motion and gain kinetic energy nonadiabatically under the influence of the strong dawn-to-dusk electric field.

4.2.2. Case II

Figure 9 summarizes snapshots of the differential flux j at the energy intervals from 10 to 50 keV (top row),

50 to 150 keV (middle row), and 150 to 350 keV (bottom row). The flux appears to increase in and westward of the region where $|E_y|$ is large at $t = 0$. At the energy interval from 10 to 50 keV, the flux is shown to increase earthward and tailward of the NENL at $\sim 11.5 R_E$. At the energy interval from 50 to 150 keV, the flux enhancement takes place earthward of the NENL only. The pileup of the magnetic flux occurs on the earthward side of the NENL only, so that $|E_y|$ is stronger on the earthward side of the NENL than on the tailward side. The asymmetry of the flux enhancement is obviously seen at the energy interval from 50 to 150 keV. At the energy interval from 150 to 350 keV, the flux appears to largely increase at $t = 4$ min.

To understand the acceleration and transport processes of the O^+ ions that reach the energy interval from 150 to 350 keV, Figure 10 shows trajectories of the 120 most significant test particles that contribute to the flux j at the energy interval from 150 to 350 keV at $X = -8.0 R_E$, $Y = 0.7 R_E$. In total, they contribute to 5% of the flux j at that point. The ions are found to depart at $(-8, -2, 2) R_E$ at $t = -4$ min with initial energy of around 5 eV. After the departure, the O^+ ions gain kinetic energy largely when it traverses the region where $|E_y|$ is large. Finally, the energy reaches ~ 300 keV. The ions undergo nonadiabatic motion because the ratio K is 0.15 for the O^+ ions with 100 keV at $X = -10 R_E$, $Y = 0$. Obviously, the trajectories of the ions do not show regular Larmor motion.

4.2.3. Time-Energy Spectrograms

Figure 11 shows energy versus time spectrograms of the differential flux of the O^+ ions at fixed positions ($5.5, 6.0$, and $7.0 R_E$; 21:00, 22:00, 23:00, and 00:00 magnetic local times (MLTs); the equatorial plane) for Case II. At $5.5 R_E$, the flux is enhanced at energy less than ~ 70 keV. The flux does not always increase simultaneously at all energies. At 23:00 MLT (Figure 11b), the flux between ~ 25 keV and ~ 60 keV increases first at $t = 7$, followed by the high energy and lower energy. The energy-time structure is similar to the nose dispersion that the flux increase is observed first at narrow energy range and spreads to both higher and lower energies [Smith and Hoffman, 1974; Ejiri *et al.*, 1980]. At 22:00 MLT (Figure 11c), the energy-time dispersion becomes significant. At 21:00 MLT (Figure 11d), the flux of the ~ 10 keV ions start to increase at $t \sim 57$ min.

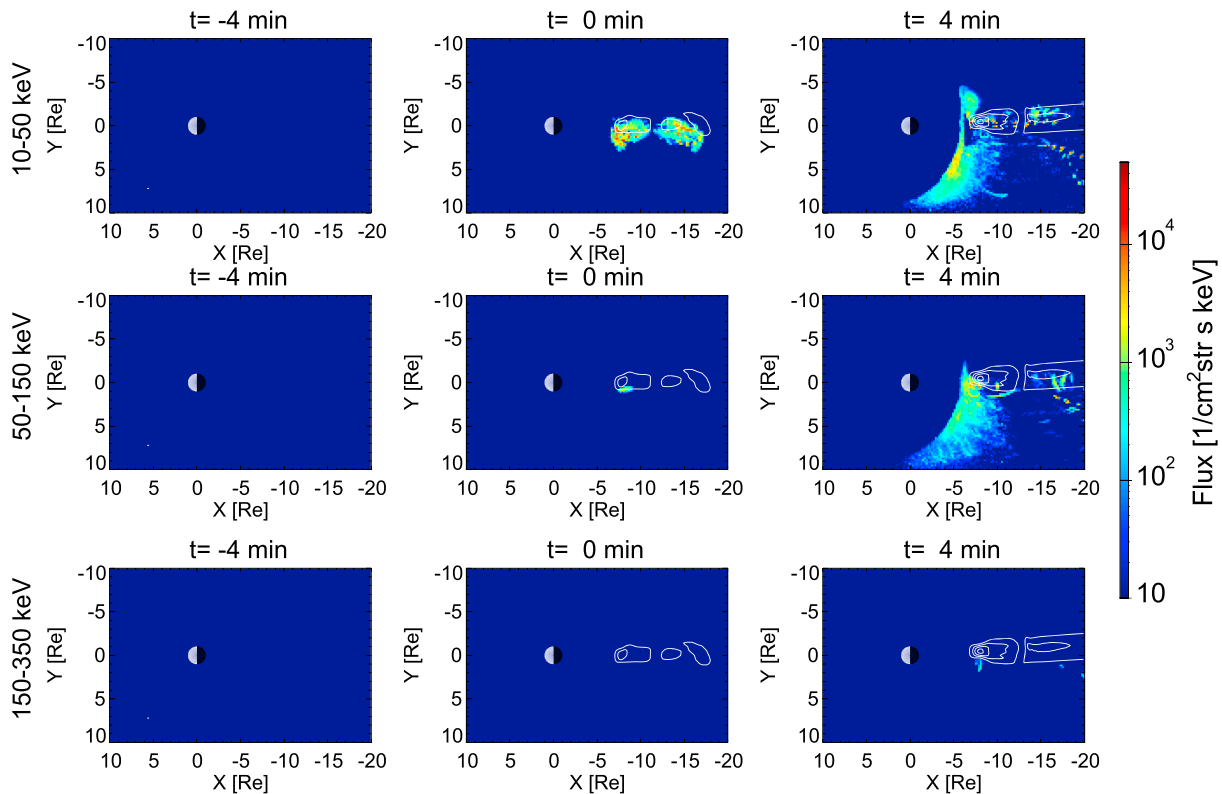


Figure 9. Same as Figure 7 except at three energy intervals from (top row) 10 to 50 keV, (middle row) 50 to 150 keV, and (bottom row) 150 to 350 keV at (first column) $t = -4$, (second column) 0, and (third column) 4 min for Case II.

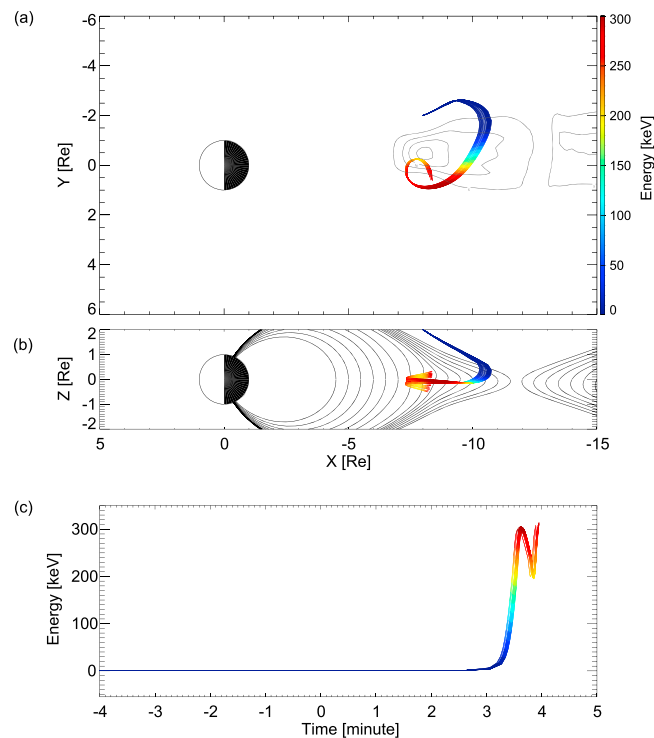


Figure 10. Same as Figure 8 except for the 120 test particles of Case II.

At $6.0 R_E$, the intensity of the flux is larger than at $5.5 R_E$. At 00:00 MLT (Figure 11e), the flux increases almost simultaneously at energy between 10 and 120 keV at $t = 0$ –1 min. High-energy (>120 keV) ion flux appears later. An isolated energy dispersion structure, energy decreasing with time, appears at $t = 35$ min and onward. This is called a drift echo, arising from the ions that encircle the Earth by the grad-B and curvature drift. At 23:00 MLT, a clear nose dispersion starts to appear at $t = 0$. At 22:00 and 21:00 MLT, the flux increases at $t = 1$ min and $t = 3$ min, respectively.

At $7.0 R_E$, the flux starts to increase at $t = 3, 3, -2$, and -1 min at 00:00, 23:00, 22:00, and 21:00 MLT, respectively. The flux of high-energy ions (>100 keV) remains, and the flux of lower energy ions (<100 keV) disappears. There is a clear discontinuity in the flux around 100 keV. As far as we know, similar energy-time spectra have not been

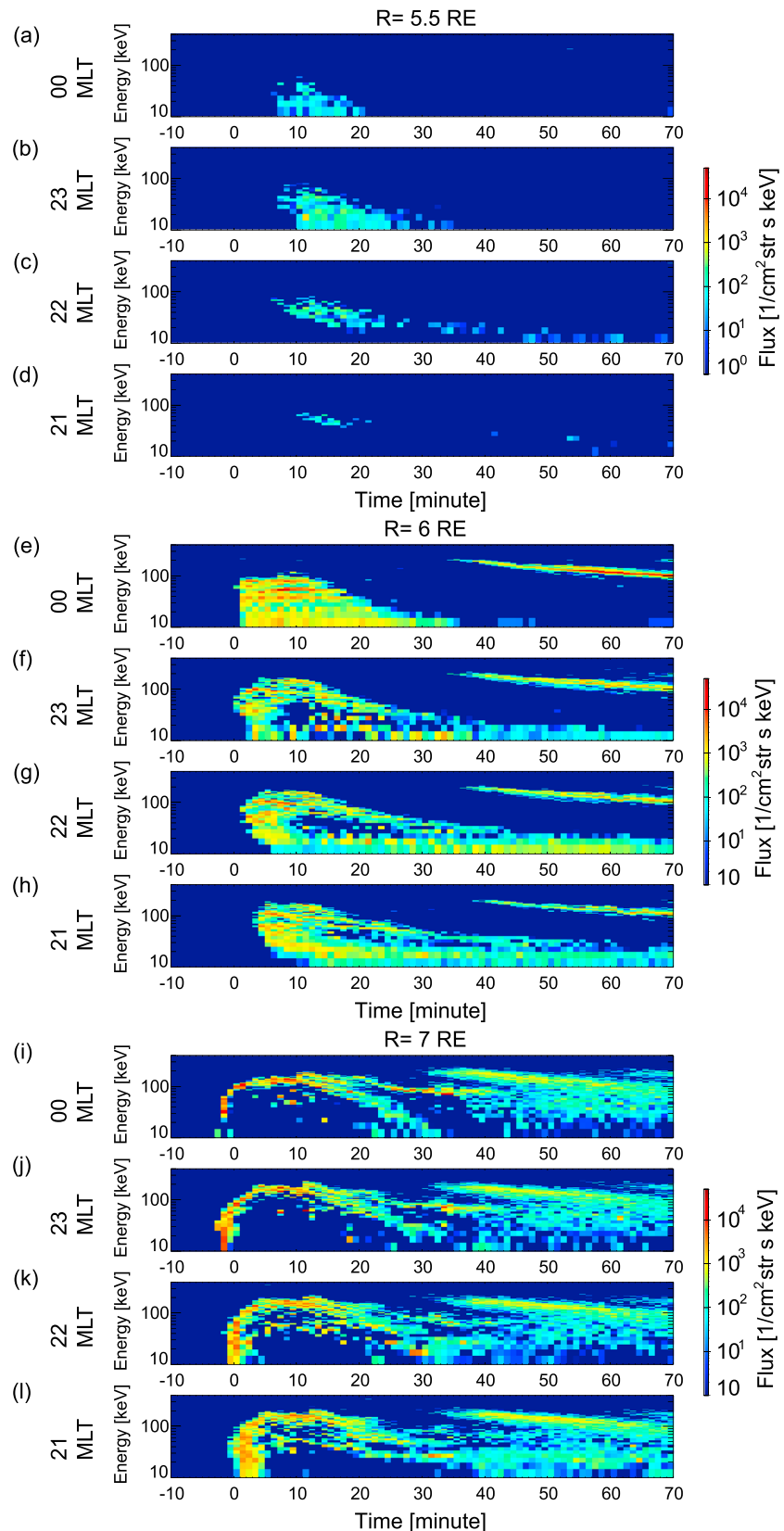


Figure 11. Energy versus time spectrograms of the differential flux of the O^+ ions at fixed positions (5.5, 6.0, and 7.0 R_E ; 21:00, 22:00, 23:00, and 00:00 MLTs; the equatorial plane) for Case II.

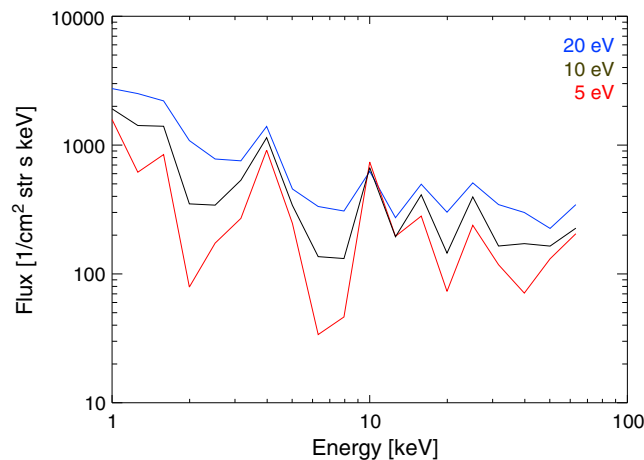


Figure 12. Differential flux j of the O^+ ions as a function of energy at 00:00 MLT and at $6 R_E$ and at $t = 5$ min. The red, black, and blue lines indicate the flux with the initial temperature of 5, 10, and 20 eV.

5 eV to 10 eV. There is also a tendency that the spectral shape is independent of the initial temperature for this particular range of temperature.

5. Discussion

The O^+ ions are accelerated by the dawn-to-dusk electric field (E_y) from the order of eV to the order of tens-of-keV range and more in the near-Earth plasma sheet. This is consistent with previous simulation studies [Cladis and Francis, 1992; Delcourt, 2002; Fok et al., 2006; Ashour-Abdalla et al., 2009; Birn et al., 2013]. At the onset of substorm expansion, the peak of E_y takes place about 1–2 R_E earthward of that of the earthward plasma flow (V_x). This misalignment is a natural consequence of the MHD process, in which the strength of the magnetic field is stronger in the inner region than in the outer region because of pileup of a magnetic flux. The pileup seems not to be simply caused by flow braking under the competition between the tension force and the magnetic pressure force. First, the plasma is accelerated earthward by the tension force near the NENL. Plasma pressure force and magnetic pressure force also participate in the action of the plasma at $\sim 8 R_E$ (in which E_y becomes large). It is emphasized that the intense acceleration of the O^+ ions occurs due to the joint action of the tension force that accelerates plasma earthward and the pressure force (including the plasma pressure force and the magnetic pressure force) that results in magnetic flux pileup.

As shown in Figure 11, the energy-time spectrograms of the differential flux of the O^+ ions strongly depend on the radial distance and MLT. At 5.5 and 6.0 R_E , the flux is enhanced at or just after the onset, and remains high for at least 10 min. The flux enhancement starts to appear at certain energy, followed, by lower and higher energies. This structure is similar to that known as “nose” dispersion [Smith and Hoffman, 1974] and can be explained by travel time and path of newly injected ions [Ejiri et al., 1980]. That is, the ions with certain energy penetrate deeper and faster into the inner region [Ejiri, 1978]. These energy versus time spectrograms shown in Figure 11 are consistent with the Explorer 45 observations [Smith and Hoffman, 1974; Ejiri et al., 1980] and the CRRES observations [Fu et al., 2002]. At 7.0 R_E , the energy-time dispersion is different. After an abrupt increase in the flux, only the flux of the ions with high energy remains. A void region, in which the flux is much lower than ambient, appears in the energy-time spectrogram. The void structure can be caused by the quasi-electrostatic acceleration of unmagnetized ions traveling through the electric potential perpendicular to the magnetic field. If the ions are magnetized, the void structure will disappear because of the following reason: When the ions undergo regular drift motion and the electric and magnetic fields are stationary, the rate of the energy change of a charged particle is given by

$$\frac{dK}{dt} = q \mathbf{v}_d \cdot \mathbf{E}, \quad (11)$$

where \mathbf{v}_d is the grad-B and curvature drift velocity. In an extremely case, a zero-energy ion will not gain kinetic energy because the grad-B and curvature drift velocity are zero. Hence, the distribution function

reported in the near-Earth plasma sheet. We call this a “void” structure and discuss it later.

4.2.4. Dependence of Flux on Initial Temperature

Figure 12 shows the differential flux j of the O^+ ions as a function of energy at 00:00 MLT and at $6 R_E$ and at $t = 5$ min. The red, black, and blue lines indicate the flux with the initial temperature of 5, 10, and 20 eV. The black line is the same as a cut of Figure 6e. The flux shows some humps because of insufficient statistics. There is a tendency that the flux increases with the initial temperature. For example, at 2 keV, the flux is doubled when the initial temperature is increased from

(and the flux) of the zero-energy ions will be unchanged according to Liouville's theorem; that is, the void structure will not be formed. Similar void structures are seen in the energy-time spectrograms observed by the Polar satellite at $L \sim 6.5\text{--}9.0$ near midnight (Figure 1). The flux has a peak at a 15–30 keV, and the flux of the ions with energy less than that energy is lower than ambient. The situation would be similar to that found in the auroral ionosphere where electrons are accelerated by quasi-electrostatic electric field directing upward, known as an “inverted-V” structure [e.g., Frank and Ackerson, 1971; Evans, 1974; Ergun et al., 2005]. In the simulation, the flux is absent before the void structure appears, whereas in the observation, the flux is relatively high before the void structure appears. The difference between the simulation and the observation can be explained by the existence of the preexisting hot ions near the plasma sheet. We have no such preexisting hot ions in the simulation domain. Although we need more careful diagnosis of the observed void structure, the void structure would be regarded as a new class of manifestation of the perpendicular acceleration of unmagnetized ions in the near-Earth plasma sheet.

Comparing the results of the two cases (Case I and Case II), we found that the degree of the acceleration of the O^+ ions is larger when the solar wind is fast and the southward IMF is strong. The reason would be that the intensity of E_y is large at $\sim 8 R_E$ in Case II, so that the ions are more effectively accelerated than in Case I. The ultimate reason why the intensity of E_y is larger in Case II than in Case I will be investigated in the near future.

6. Conclusion

We obtained the following major conclusions.

1. Near an onset of substorm expansion, strong dawn-to-dusk electric field E_y is produced at $\sim 7.5\text{--}8.0 R_E$ by a joint action of the fast earthward flow V_x (due to the tension force) and magnetic flux pileup (due to the plasma pressure force and the magnetic pressure force). The peak of E_y is located at $\sim 7.5\text{--}8.0 R_E$ and is located $\sim 1\text{--}2 R_E$ earthward of the peak of V_x . The misalignment comes from pileup of a magnetic flux.
2. O^+ ions with energy on the order of eV are nonadiabatically accelerated to higher than 100 keV by the strong E_y in ~ 10 min. As a consequence, a void structure appears in the energy versus time spectrogram of the ion flux. This is consistent with the Polar satellite observation. The void structure would be a manifestation of the perpendicular acceleration of unmagnetized ions.
3. In the inner magnetosphere (at $5.5 R_E$ and $6.0 R_E$), a nose-dispersion appears in the energy versus time spectrogram. This is consistent with satellite observations. It is shown that outflowing O^+ ions can be a direct source of the nose-dispersion seen in the inner magnetosphere.
4. The O^+ ions are more effectively accelerated when the solar wind is fast and the southward IMF is strong.

Acknowledgments

Computation in the present study was performed with the KDK system of Research Institute for Sustainable Humanosphere at Kyoto University as a collaborative research project. This study was supported by KAKENHI, Grant-in-Aid for Scientific Research (B) 24340119. We thank Theodore A. Fritz and Manuel Grande for providing us valuable data from Polar/MICS.

Larry Kepko thanks Mei-Ching Fok and another reviewer for their assistance in evaluating this paper.

References

- Ashour-Abdalla, M., J. M. Boaqued, M. El-Alaoui, V. Peromian, M. Zhou, R. Richard, R. Walker, A. Runov, and V. Angelopoulos (2009), A simulation study of particle energization observed by THEMIS spacecraft during a substorm, *J. Geophys. Res.*, *114*, A09204, doi:10.1029/JA014126.
- Birn, J., M. Hesse, R. Nakamura, and S. Zaharia (2013), Particle acceleration in depolarization events, *J. Geophys. Res. Space Physics*, *118*, 1960–1971, doi:10.1002/jgra.50132.
- Cladis, J. B., and W. E. Francis (1992), Distribution in magnetotail of O^+ ions from cusp/cleft ionosphere: A possible substorm trigger, *J. Geophys. Res.*, *97*(A1), 123–130, doi:10.1029/91JA02376.
- Daglis, I. A. (1997), The role of magnetosphere-ionosphere coupling in magnetic storm dynamics, in *Magnetic Storm, Geophys. Monogr. Ser.*, vol. 98, edited by B. T. Tsurutani et al., pp. 107–116, AGU, Washington, D. C.
- Daglis, I. A., and W. L. Axford (1996), Fast ionospheric response to enhanced activity in geospace: Ion feeding of the inner magnetotail, *J. Geophys. Res.*, *101*, 5047–5065, doi:10.1029/95JA02592.
- Daglis, I. A., E. T. Sarris, and B. Wilken (1993), AMPTE/CCE CHEM observations of the ion population at geosynchronous altitudes, *Ann. Geophys.*, *11*, 685.
- Delcourt, D. C. (2002), Particle acceleration by inductive electric fields in the inner magnetosphere, *J. Atmos. Terr. Phys.*, *64*, 551–559.
- Delcourt, D. C., and T. E. Moore (1992), Precipitation of ions induced by magnetotail collapse, *J. Geophys. Res.*, *97*(A5), 6405–6415, doi:10.1029/91JA03142.
- Delcourt, D. C., J. A. Sauvaud, and T. E. Moore (1990), Cleft O^+ contribution to the ring current, *J. Geophys. Res.*, *95*, 20,937–20,943, doi:10.1029/JA095iA12p20937.
- Delcourt, D. C., T. E. Moore, and J. A. Sauvaud (1991), Gyro-phase effects near the storm time boundary of energetic plasma, *Geophys. Res. Lett.*, *18*(8), 1485–1488, doi:10.1029/91GL01526.
- Ebihara, Y., and T. Tanaka (2013), Fundamental properties of substorm-time energetic electrons in the inner magnetosphere, *J. Geophys. Res. Space Physics*, 1589–1603, doi:10.1002/jgra.50115.
- Ebihara, Y., M. Yamada, S. Watanabe, and M. Ejiri (2006), Fate of outflowing suprathermal oxygen ions that originate in the polar ionosphere, *J. Geophys. Res.*, *111*, A04219, doi:10.1029/2005JA011403.
- Ejiri, M. (1978), Trajectory traces of charged particles in the magnetosphere, *J. Geophys. Res.*, *83*(A10), 4798–4810, doi:10.1029/JA083iA10p04798.

- Ejiri, M., R. Hoffman, and P. H. Smith (1980), Energetic particle penetrations into the inner magnetosphere, *J. Geophys. Res.*, **85**(A2), 653–663, doi:10.1029/JA085iA02p00653.
- Elliott, H. A., J. Jahn, C. J. Pollock, T. E. Moore, and J. L. Horwitz (2007), O^+ transport across the polar cap, *J. Atmos. Sol. Terr. Phys.*, **69**, 1541–1555, doi:10.1016/j.jastp.2007.06.003.
- Ergun, R. E., L. Andersson, Y.-J. Su, D. L. Newman, M. V. Goldman, W. Lotko, C. C. Chaston, and C. W. Carlson (2005), Localized parallel electric fields associated with inertial Alfvén waves, *Phys. Plasmas*, **12**, 07290, doi:10.1063/1.1924495.
- Evans, D. S. (1974), Precipitating electron fluxes formed by a magnetic field aligned potential difference, *J. Geophys. Res.*, **79**(19), 2853–2858, doi:10.1029/JA079i019p02853.
- Fok, M. C., T. E. Moore, P. C. Brandt, D. C. Delcourt, S. P. Slinker, and J. A. Fedder (2006), Impulsive enhancements of oxygen ions during substorms, *J. Geophys. Res.*, **111**, A10222, doi:10.1029/2006JA011839.
- Frank, L. A., and K. L. Ackerson (1971), Observations of charged particle precipitation into the auroral zone, *J. Geophys. Res.*, **76**(16), 3612–3643, doi:10.1029/JA076i016p03612.
- Fu, S. Y., Q. G. Zong, T. A. Fritz, Z. Y. Pu, and B. Wilken (2002), Composition signatures in ion injections and its dependence on geomagnetic conditions, *J. Geophys. Res.*, **107**(A10), 1299, doi:10.1029/2001JA002006.
- Hamilton, D. C., G. Gloeckler, F. M. Ipavich, W. Studemann, B. Wilken, and G. Kremser (1988), Ring current development during the great geomagnetic storm of February 1986, *J. Geophys. Res.*, **93**, 14,343–14,355, doi:10.1029/JA093iA12p14343.
- Keika, K., P. C. Brandt, S. Ohtani, D. G. Mitchell, K. Min, M. Nose, T. Obara, H. Koshiishi, and H. Matsumoto (2010), Mass-dependent evolution of energetic neutral atoms energy spectra during storm time substorms: Implication for O^+ nonadiabatic acceleration, *J. Geophys. Res.*, **115**, A00112, doi:10.1029/2010JA015889.
- Kistler, L. M., F. M. Ipavich, D. C. Hamilton, G. Gloeckler, B. Wilken, G. Kremser, and W. Stüdemann (1989), Energy spectra of the major ion species in the ring current during geomagnetic storms, *J. Geophys. Res.*, **94**(A4), 3579–3599, doi:10.1029/JA094iA04p03579.
- Kistler, L. M., C. G. Mouikis, B. Klecker, and I. Dandouras (2010), Cusp as a source for oxygen in the plasma sheet during geomagnetic storms, *J. Geophys. Res.*, **115**, 3209, doi:10.1029/2009JA014838.
- Krimigis, S. M., G. Gloeckler, R. W. McEntire, T. A. Potemra, F. L. Scarf, and E. G. Shelley (1985), Magnetic storm of September 4, 1984: A synthesis of ring current spectra and energy densities measured with AMPTE/CCE, *Geophys. Res. Lett.*, **12**, 329–332, doi:10.1029/GL012i005p00329.
- Lennartsson, W., E. G. Shelley, R. D. Sharp, and R. G. Johnson (1979), Some initial ISEE-1 results on the ring current composition and dynamics during the magnetic storm of December 11, 1977, *Geophys. Res. Lett.*, **6**, 483–486, doi:10.1029/GL006i006p00483.
- Liao, J., L. M. Kistler, C. G. Mouikis, B. Klecker, I. Dandouras, and J.-C. Zhang (2010), Statistical study of O^+ transport from the cusp to the lobes with cluster codif data, *J. Geophys. Res.*, **115**, A00J15, doi:10.1029/2010JA015613.
- Lundin, R., B. Hultqvist, N. Pissarenko, and A. Zacharov (1982), The plasma mantle: Composition and other characteristics observed by means of the Prognoz-7 satellite, *Space Sci. Rev.*, **31**, 247.
- Mitchell, D. G., P. C. Brandt, E. C. Roelof, D. C. Hamilton, K. C. Retterer, and S. Mende (2003), Global imaging of O^+ from IMAGE/HENA, *Space Sci. Rev.*, **109**, 63–75.
- Moore, T. E., and D. C. Delcourt (1995), The geopause, *Rev. Geophys.*, **33**, 175–209, doi:10.1029/95RG00872.
- Moore, T. E., et al. (1997), High-altitude observations of the polar wind, *Nature*, **277**, 349.
- Moore, T. E., R. Lundin, D. Alcayde, M. André, S. B. Ganguli, M. Temerin, and A. Yau (1999), Source processes in the high-latitude ionosphere, *Space Sci. Rev.*, **88**(1–2), 7–84.
- Moore, T. E., M. O. Chandler, M.-C. Fok, B. L. Giles, D. C. Delcourt, J. L. Horwitz, and C. J. Pollock (2001), Ring current and internal plasma sources, *Space Sci. Rev.*, **95**, 555–568.
- Nakayama, Y., Y. Ebihara, and T. Takashi (2014), Simulation of substorm-time acceleration of oxygen ions on azimuthally directed magnetic field lines in the near-Earth plasma sheet, *J. Geophys. Res. Space Physics*, **119**, 6167–6176, doi:10.1002/2014JA019858.
- Nilsson, H., et al. (2004), The structure of high altitude O^+ energization and outflow: A case study, *Ann. Geophys.*, **22**, 2497.
- Nose, M., S. Ohtani, K. Takahashi, A. T. Y. Lui, R. W. McEntire, D. J. Williams, S. P. Christon, and K. Yumoto (2001), Ion composition of the near-Earth plasma sheet in storm and quiet intervals: Geotail/EPIC measurements, *J. Geophys. Res.*, **106**, 8391–8404, doi:10.1029/2000JA000376.
- Ohtani, S., P. C. Brandt, D. G. Mitchell, H. Singer, M. Nosé, G. D. Reeves, and S. B. Mende (2005), Storm-substorm relationship: Variations of the hydrogen and oxygen energetic neutral atom intensities during storm-time substorms, *J. Geophys. Res.*, **110**, A07219, doi:10.1029/2004JA010954.
- Ohtani, S., et al. (2007), Cluster observations in the magnetosphere during the 18 April 2002 sawtooth event: Dipolarization and injection at $r = 4.6 R_E$, *J. Geophys. Res.*, **112**, A08213, doi:10.1029/2007JA012357.
- Ohtani, S., M. Nosé, Y. Miyashita, and A. T. Y. Lui (2015), Responses of different ion species to fast plasma flows and local dipolarization in the plasma sheet, *J. Geophys. Res. Space Physics*, **120**, 187–200, doi:10.1002/2014JA020517.
- Peromian, V., M. El-Alaoui, and P. C. Brandt (2011), The ion population of the magnetotail during the 17 April 2002 magnetic storm: Large-scale kinetic simulations and IMAGE/HENA observations, *J. Geophys. Res.*, **116**, A05214, doi:10.1029/2010JA016253.
- Roeder, J. L., J. F. Fennell, M. W. Chen, M. Schulz, M. Grande, and S. Livi (1996), CRRES observations of the composition of the ring-current ion populations, *Adv. Space Res.*, **17**(10), 17–24.
- Sergeev, V. A., E. M. Sazhina, N. A. Tsyganenko, J. A. Lundblad, and F. Soraas (1983), Pitch-angle scattering of energetic protons in the magnetotail current sheet as the dominant source of their isotropic precipitation into the ionosphere, *Planet. Space Sci.*, **31**, 1147.
- Shelley, E. G., R. G. Johnson, and R. D. Sharp (1972), Satellite observations of energetic heavy ions during a geomagnetic storm, *J. Geophys. Res.*, **77**, 6104–6110, doi:10.1029/JA077i031p06104.
- Smith, P. H., and R. A. Hoffman (1974), Direct observation in the dusk hours of the characteristics of the storm time ring current particles during the beginning of magnetic storms, *J. Geophys. Res.*, **79**, 966–967, doi:10.1029/JA079i007p00966.
- Summers, D., and M. Thorne (1991), The modified plasma dispersion function, *Phys. Plasmas*, **3**, 1835, doi:10.1063/1.859653.1.
- Tanaka, T., A. Nakamizo, A. Yoshikawa, S. Fujita, H. Shinagawa, H. Shimizu, T. Kikuchi, and K. K. Hashimoto (2010), Substorm convection and current system deduced from the global simulation, *J. Geophys. Res.*, **115**, A05220, doi:10.1029/JA014676.
- Vasyliunas, V. M. (1968), A survey of low-energy electrons in the evening sector of the magnetosphere with OGO 1 and OGO 3, *J. Geophys. Res.*, **73**, 2839–2884, doi:10.1029/JA073i009p02839.
- Wilken, B., et al. (1992), Magnetospheric ion composition spectrometer onboard the CRRES spacecraft, *J. Spacecr. Rockets*, **29**, 585–591.
- Young, D. T., H. Balsiger, and J. Geiss (1982), Correlations of magnetospheric ion composition with geomagnetic and solar activity, *J. Geophys. Res.*, **87**, 9077–9096, doi:10.1029/JA087iA11p09077.
- Zong, Q.-G., et al. (1997), Geotail observations of energetic ion species and magnetic field in plasmod-like structures in the course of an isolated substorm event, *J. Geophys. Res.*, **102**(A6), 11,409–11,428, doi:10.1029/97JA00076.